Catalysis Letters 60 (1999) 113–120

High-resolution imaging of nanoparticle bimetallic catalysts supported on mesoporous silica

Dogan Ozkaya [a], Wuzong Zhou [b], John Meurig Thomas [a,c,*], Paul Midgley [a], Vicki J. Keast [a] and Sophie Hermans [b]

[a] *Department of Materials Science and Metallurgy, University of Cambridge, New Museums Site, Pembroke Street, Cambridge CB2 3QZ, UK*
[b] *Department of Chemistry, University of Cambridge, Lensfield Road, Cambridge CB2 1EW, UK*
[c] *Davy–Faraday Research Laboratory, The Royal Institution of Great Britain, 21 Albemarle Street, London W1X 4BS, UK*

Received 13 March 1999; accepted 27 April 1999

Although conventional high-resolution transmission electron microscopy is a powerful method for the elucidation of the structure of mesoporous solids (diameter of pores from 1.5 to 20 nm), it is far less capable than high-resolution scanning transmission electron microscopy in identifying the spatial distribution of nanocrystals of catalysts encapsulated within the mesopores. Using high-angle annular dark-field imaging (either in a 100 or 300 keV STEM system), it is possible to locate precisely individual bimetallic nanoparticles (Ag_3Ru_{10}, Cu_4Ru_{12} and Pd_6Ru_6 hydrogenation catalysts) supported on mesoporous silica, to determine their size distribution, and to record their characteristic X-ray emission maps. It is also established that there is little tendency for elemental fragmentation of the bimetallic catalysts, all of which were prepared by decarbonylating, by thermolysis, precursor cluster carbonylate anions: $[Ag_3Ru_{10}C_2(CO)_{28}Cl]^-$, $[Ru_6C(CO)_{16}Cu_2Cl]^{2-}$ and $[Ru_6Pd_6(CO)_{24}]^{2-}$.

Keywords: bimetallic nanoparticles, Cu–Ru, Ag–Ru, Pd–Ru, Rutherford scattering, *Z*-contrast microscopy, elemental imaging, hydrogenation catalysts, X-ray emission

1. Introduction

The recent availability [1–4] of well-defined mesoporous silica has been responsible for a growing number of powerful new heterogeneous catalysts produced by the grafting of various heteroatoms on to the pendant silanol groups that line the inner surfaces of the mesopores. Not only is it possible to introduce [5,6] specific single ions, such as Ti(IV) or Mo(VI), as discrete catalytic sites (for selective oxidation) on to the inner surface of the high-area mesoporous silica (especially the variant known as MCM-41), but it has also been feasible to anchor nanoscale bimetallic catalysts that are very effective [7,8] in a range of hydrogenation processes.

Whereas X-ray absorption spectroscopy, perhaps alone among currently available [9] physical techniques of catalyst characterisation, is capable of defining in atomic detail the spatially averaged structure in the immediate vicinity of the active sites, for a deeper understanding of the catalytic performance of bimetallic nanoparticles, high-resolution electron microscopy [7–12] (HREM), aided by electron-stimulated methods of elemental analysis, is indispensable. X-ray diffraction is relatively less useful in the context of the characterisation of mesoporous silica than it is for most other solids, unlike HREM which provides unambiguous information pertaining to pore dimensions, short-range and long-range crystallographic order of the mesoporous silica and the nature of specific (e.g., defective) regions of the sample. Insofar as the bimetallic nanoparticles anchored inside the pores of the silica are concerned, HREM is indisputably the single most effective tool for their characterisation. Here, we illustrate the veracity of the above statements by reference to a number of active, supported catalysts, fuller details of the preparation and performance of which are given elsewhere [7,8,11,13].

2. A suite of bimetallic catalysts encapsulated within mesoporous silica

The kind of bimetallic catalyst described [7,8,13] in recent publications are those that smoothly hydrogenate alkenes such as hex-1-ene, diphenylacetylene, phenylacetylene, stilbene, *cis*-cyclooctene, naphthalene and D-limonene. Nominally, these have compositions such as Ag_3Ru_{10}, Cu_4Ru_{12} and Pd_6Ru_6. All of them are prepared by introducing the mixed-metal cluster carbonylate into the mesoporous MCM-41 silica. The carbonyl groups of the mixed-metal cluster anions, as well as the organic charge-compensating cation (see below), are then driven off by mild thermolysis (monitored by *in situ* Fourier transform infrared spectroscopy [7,8]) leaving the denuded bimetallic nanocrystals anchored to the siliceous substratum. Extended X-ray absorption fine structure (EXAFS) analysis of the structure of Ag_3Ru_{10} and Cu_4Ru_{12} shows that the clusters are anchored firmly to the silica, via oxygen atoms that are covalently bonded to oxophilic Ag (or Cu) atoms.

* To whom correspondence should be addressed.

For the Ag_3Ru_{10} (anchored) bimetallic catalysts, the precursor anion is $[Ag_3Ru_{10}C_2(CO)_{28}Cl]^-$ and its charge-compensating ion is PPN^+ (which stands for bis(triphenylphosphino)iminium) [7].

For the Cu_4Ru_{12} (anchored) bimetallic catalysts, the precursor anion is $[Ru_6C(CO)_{16}Cu_2Cl]^{2-}$ and PPN^+ ions are again the charge compensators [8].

For Pd_6Ru_6 (anchored) bimetallic catalysts, the precursor anion is $[Ru_6Pd_6(CO)_{24}]^{2-}$ and tetraethylammonium $[NEt_4]^+$ are the charge compensators [13].

3. HRTEM studies of MCM-41

Several detailed studies have been reported dealing with the imaging of MCM-41. This mesoporous solid may be envisaged as being composed of hexagonally stacked, hollow silica tubes, the diameters of which, depending on the precise mode of their preparation, may range between 15 and 150 Å. Typical high-resolution transmission electron microscopic (HRTEM) images are shown in figures 1 and 2. Where appropriate, we also show the corresponding diffraction pattern (Fourier transform) of the image. Figure 3 is a HRTEM image of a new mesoporous silica [4], designated STAC-1 (St. Andrews–Cambridge mesoporous silica), where cubic stacking forms instead of hexagonal stacking as in the closely related material, SBA-2 (Santa Barbara No. 2). Tese two phases were found often to be in intergrown states.

Figure 4 is a HRTEM image of MCM-41 loaded with $[Ru_6Pd_6(CO)_{24}]\{NEt_4]$ showing a rosary-like contrast pattern [11]. This clearly shows how well ordered the mixed-metal carbonylate anions are within the pores. After denuding the cluster anions of their carbonyl groups and driving off the NEt_4 cations, the resulting Pd_6Ru_6 clusters are encapsulated within the mesopores, but lack long-range order. In fact, scanning transmission electron microscopy (STEM) is a more powerful method of pin-pointing the positions taken up by these bimetallic nanoparticles than conventional HRTEM. We, therefore, briefly outline next the salient principles of this technique.

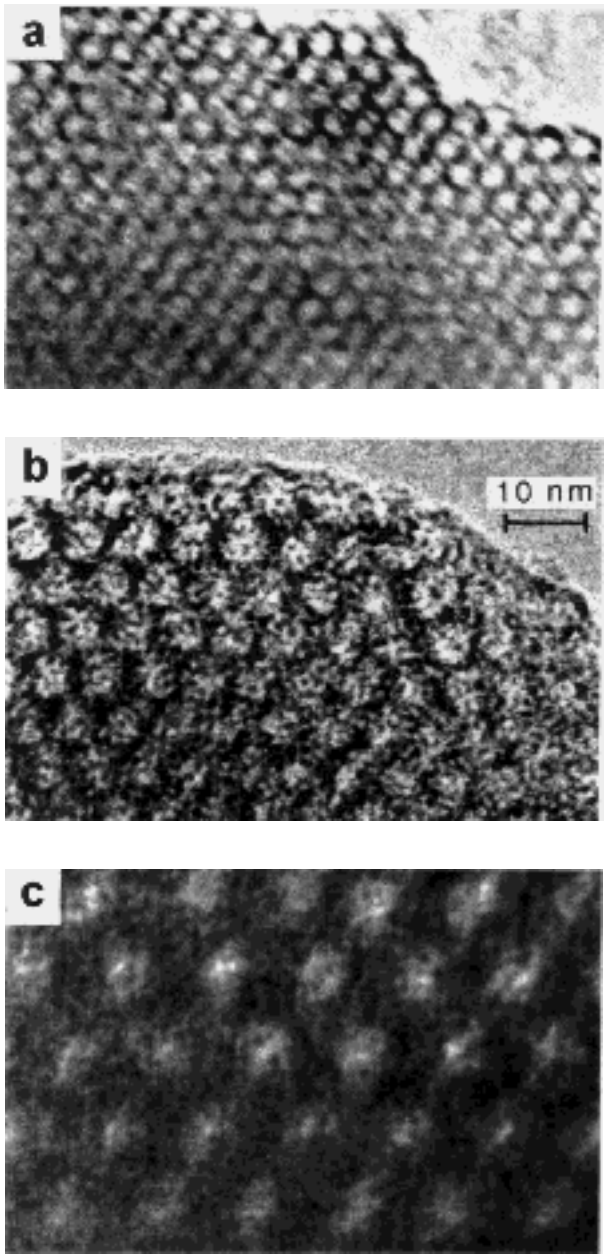

Figure 1. HRTEM images from MCM-41 with different pore sizes, viewed down the pore axis. The bright disks are the direct images of the mesopores. The inter-pore distances (centre to centre) are (a) 4.2, (b) 6.8 and (c) 12.2 nm.

4. STEM: Rutherford-scattering and Z-contrast microscopy

We first show a selection of typical STEM images taken with a Vacuum Generators VG HB 501 field-emission microscope. Figures 5 and 6 show annular dark-field views of encapsulated Ag_3Ru_{10} and Cu_4Ru_{12} nanocatalysts; and figure 7 shows how microdensitometry succeeds in distinguishing one from two superimposed nanoparticles. (For an outline of the salient experimental procedure, see [7,8,14].)

4.1. Principles of Z-contrast imaging

Images in the STEM are formed by rastering a focused probe over the specimen and at each point in the raster detecting either transmitted electrons to form a bright-field (BF) image or scattered electrons to form a dark-field (DF) image. The simple diagram of figure 8 illustrates the detector geometry found in the STEM. Conventional DF images are recorded using an annular detector placed around the BF detector. Such images are formed from electrons that have been scattered to relatively small angles. Low-angle scattered electrons are predominantly coherent and thus both BF and DF images will show phase contrast (diffraction contrast) and are thus prone to contrast reversals with changes in specimen thickness or defocus. Electrons scattered to high angles are predominantly incoherent and images

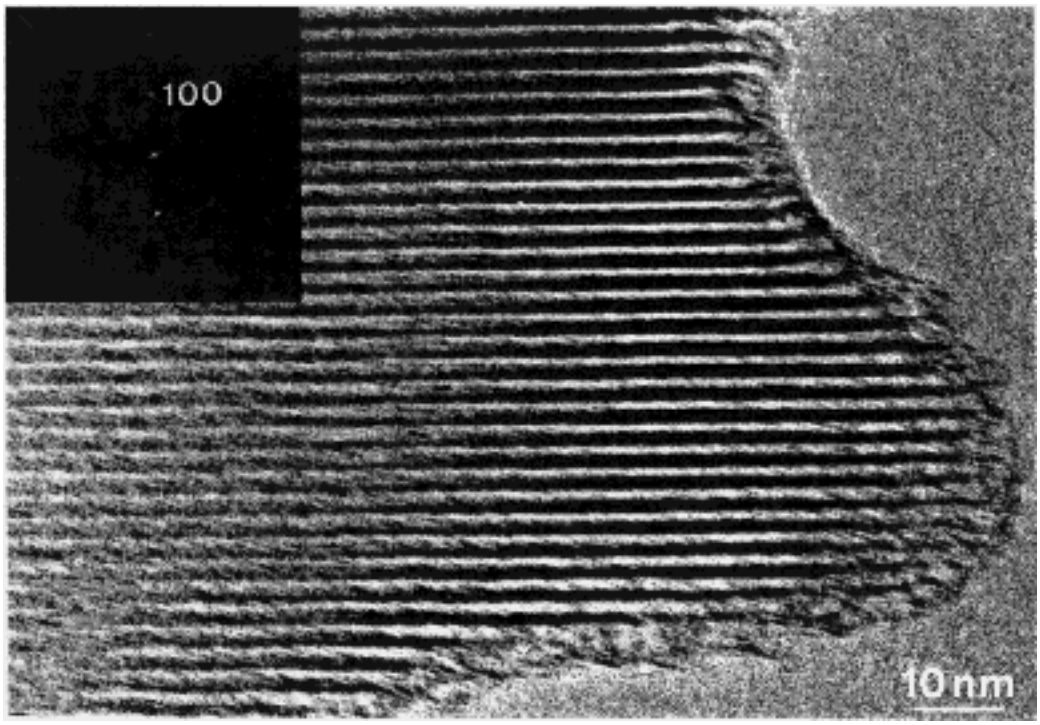

Figure 2. HRTEM image of pure silica MCM-41, along with the Fourier transform (inset), viewed perpendicular to the pore axis, along which no sign of crystallographic ordering was detected.

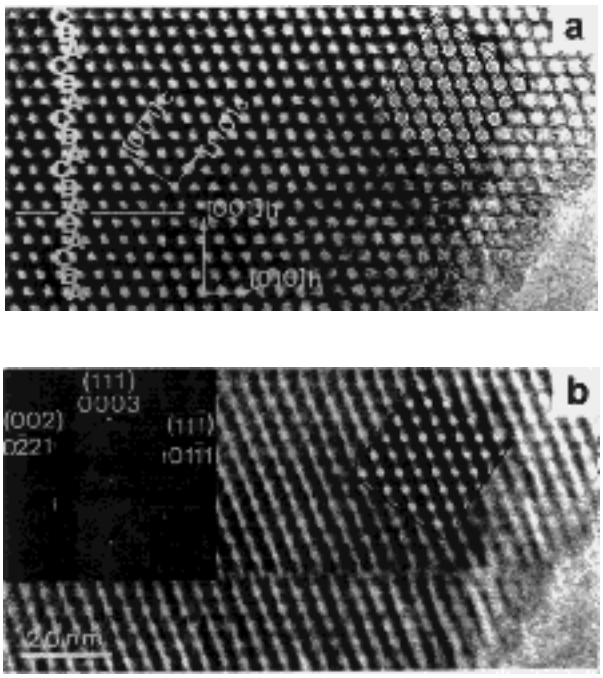

Figure 3. Underfocus (a) and overfocus (b) HRTEM images of STAC-1 viewed down the a axis of a hexagonal unit cell (indicated by $[hkl]_{\mathrm{h}}$) or the [110] direction of a cubic unit cell (indicated by $[hkl]_{\mathrm{c}}$). The crystal is dominated by "ABCABC" close packing (indicated on (a)) with one stacking fault (marked by a horizontal line on (a)). A Fourier transform optical diffraction pattern with both Miller–Bravais indices to the hexagonal unit cell and Miller indices (in parentheses) to the cubic unit cell is inserted in (b). Simulated images are also inserted with specimen thicknesses of 300 Å, and lens focusses of -300 (a) and -100 Å (b).

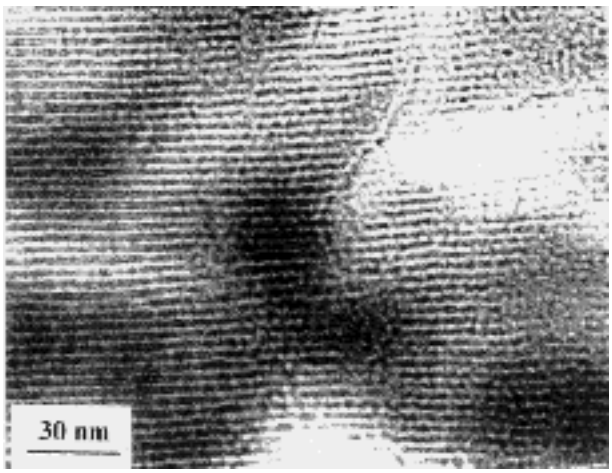

Figure 4. HRTEM image of MCM-41 loaded with $[Ru_6Pd_6(CO)_{24}]\{NEt_4\}$ prepared as described in [13].

formed using a high-angle annular dark-field (HAADF) detector [15] do not show the contrast changes associated with coherent scattering. Further, electrons scattered to such high angles must have been scattered from close to the nucleus of the atom and thus the cross-section for HAADF scattering approaches the unscreened Rutherford cross-section which is strongly dependent on the atomic number, Z; in fact, it is proportional to Z^2 [16,17]. Thus an image formed using a HAADF detector is very sensitive to changes in specimen composition and is thus an ideal way to image small nanoparticles with moderate or high atomic number on a low-Z support. The power of the STEM is that

BF and HAADF images can be acquired concurrently with other chemically-sensitive signals such as X-ray emission, as shown below.

4.2. Typical results exemplifying the merits of Z-contrast imaging

In figure 9, we show a histogram of particle-size distribution from figure 6. The particle size is taken as the full width at half maximum (FWHM) intensity in this image. Although this seems to be a widely used convention in recording particle-size distribution, the particle intensities in the image are very much affected by the differences in defocus, especially so because of the narrow depth of field in the HAADF images. This means that the particles that are at different heights within the sample have different intensity distribution, i.e., different FWHM values. The size of a particle in the image can be thought of as a convolution of the probe intensity profile with the scattering potential of the particle (a function of Z^2 and density distribution within the particle) [18]. The effect of the noise further complicates an accurate determination. If, as a first approximation, beam-broadening behaviour is considered, then, for a probe of diameter 0.5 nm focussed at the top of a 20 nm thick sample and with a beam semi-convergence of 7 mrad, the probe will defocus to a diameter of 0.78 nm. This degree of broading is more than sufficient to explain the variations of FWHM in figure 9.

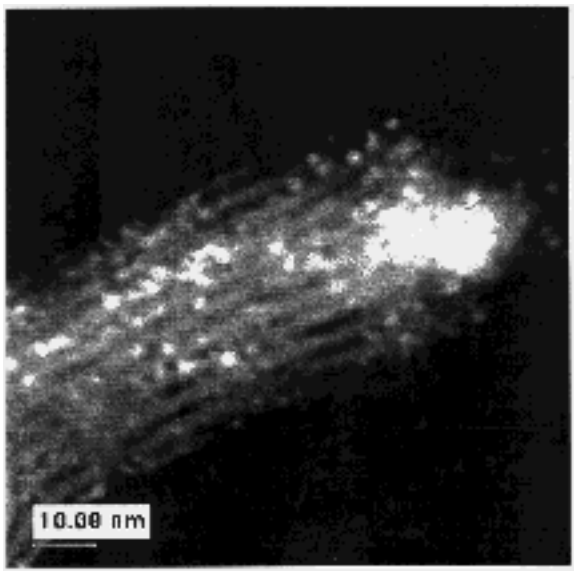

Figure 5. HAADF image (see text) of Ag_3Ru_{10} nanoparticle catalysts encapsulated inside the mesopores of MCM-41 silica.

5. Supported catalysts of Pd_6Ru_6 nanocrystals

In a separate study, principally using X-ray absorption spectroscopy [13], it has been deduced that thermolysis of the silica (MCM-41)-supported $[Pd_6Ru_6(CO)_{24}]^{2-}$ anions yield discrete clusters of Pd_6Ru_6.

In addition to HAADF images of the bimetallic (PdRu) nanocrystals, figure 10 shows images of elemental distributions, acquired by collecting the characteristic X-rays

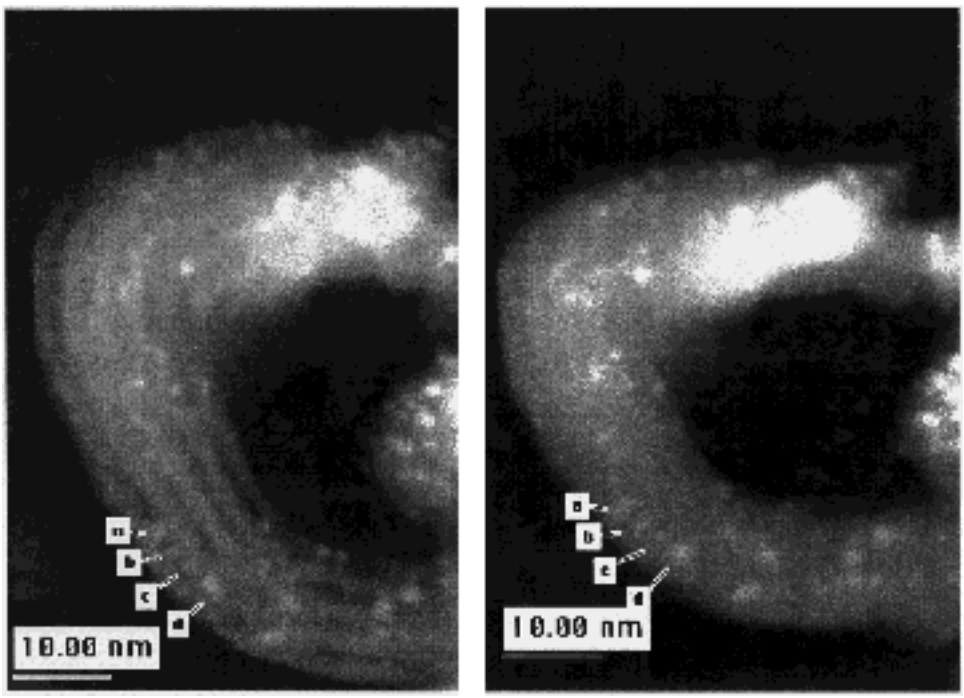

Figure 6. HAADF images of a typical specimen of Cu_4Ru_{12} nanocatalysts encapsulated in MCM-41 silica (left). Four specific particles ((a)–(d)) remain fixed in their positions even after the surrounding silica becomes amorphous during electron beam irradiation (right).

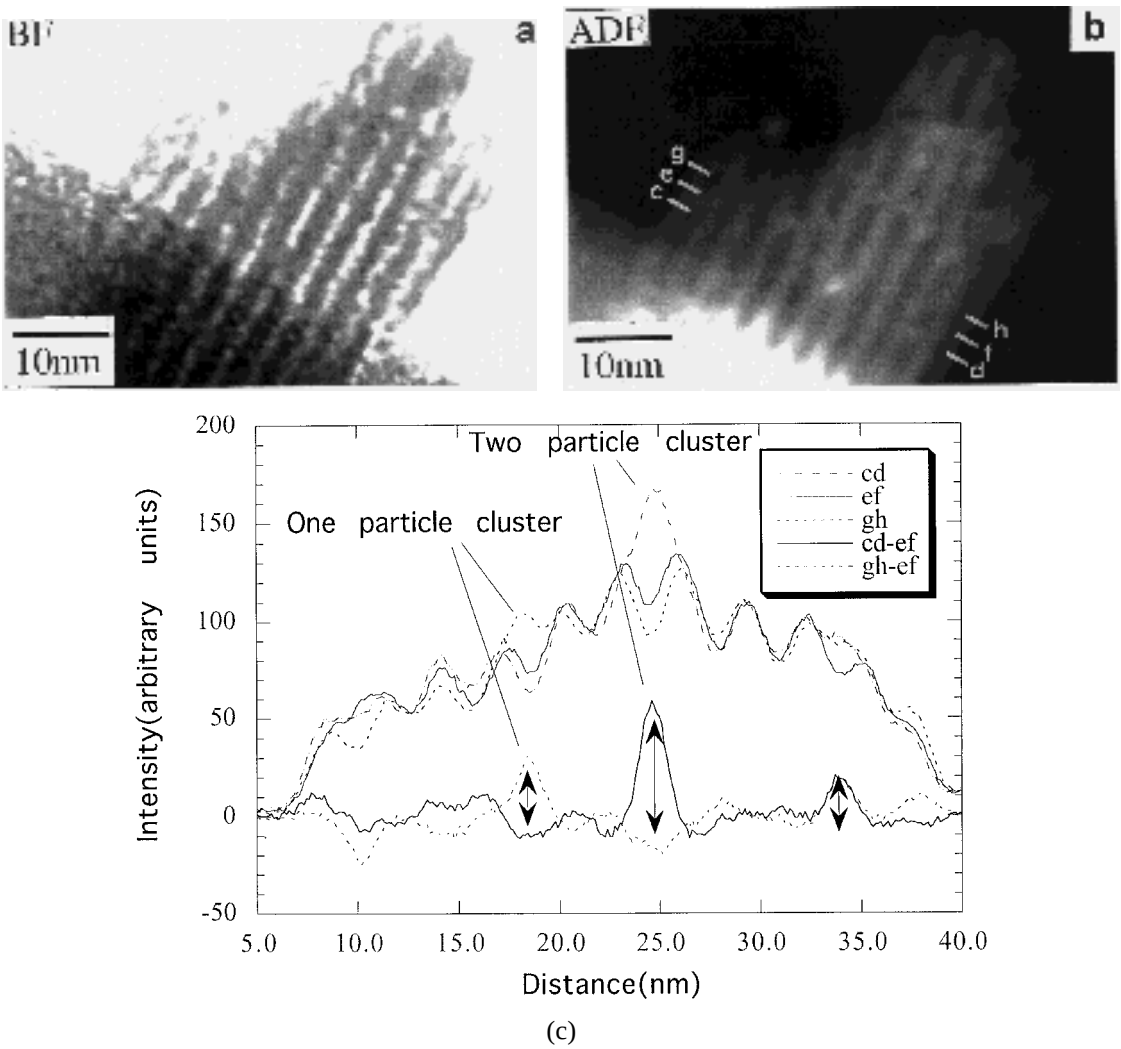

Figure 7. (a) Bright-field and (b) annular dark-field views of Ag_3Ru_{10} nanoparticles inside the channels of MCM-41. (c) Microdensitometer traces along the lines cd, ef and gh of (b). From the "difference" traces ((cd – ef) and (gh – ef)) it is readily possible to identify whether there is one or two nanoparticles superimposed inside the channels.

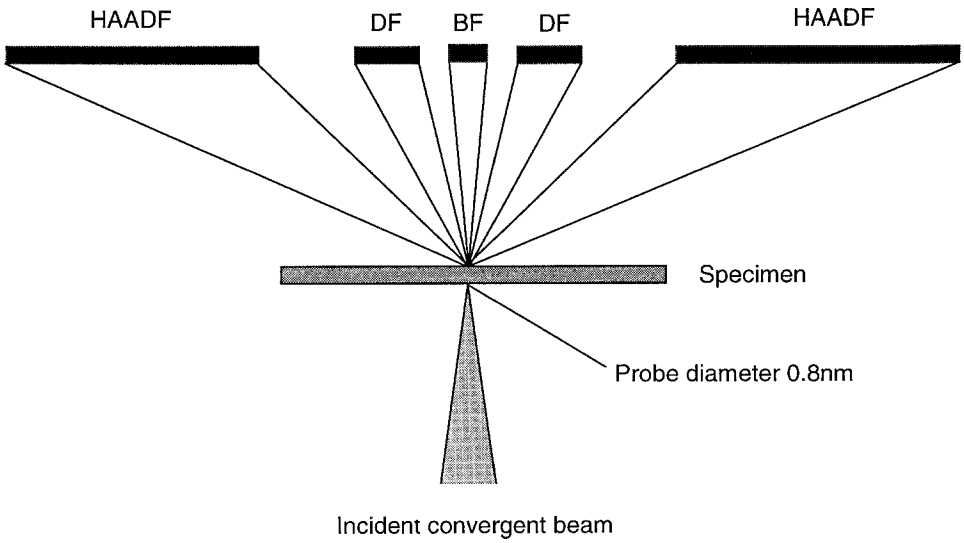

Figure 8. Schematic diagram illustrating the geometry of the detectors in the STEM. Typical detector collection angles are: BF 0–10 mrad, DF 10–50 mrad and HAADF 80–200 mrad.

emitted when the focussed electron probe interacts with the specimen. Figure 11 shows similar elemental images, acquired using a VG HB 603 STEM, along with the corresponding BF and HAADF images. The collection efficiency in the VG HB 603 is somewhat better than that in the VG HB 501 giving improved counting statistics in the elemental images and individual Pd_6Ru_6 clusters can be resolved more easily. The use of higher kinetic energy (300 keV) electrons reduces the ionisation damage rate of the siliceous samples under irradiation. This enables the pores in the mesoporous silica to be observed in the Si and O elemental images. There is also a suggestion in the Pd and Ru images that some clusters contain a greater fraction of Ru than others, although the overall compositional ratio is ca. 1 : 1 within experimental error.

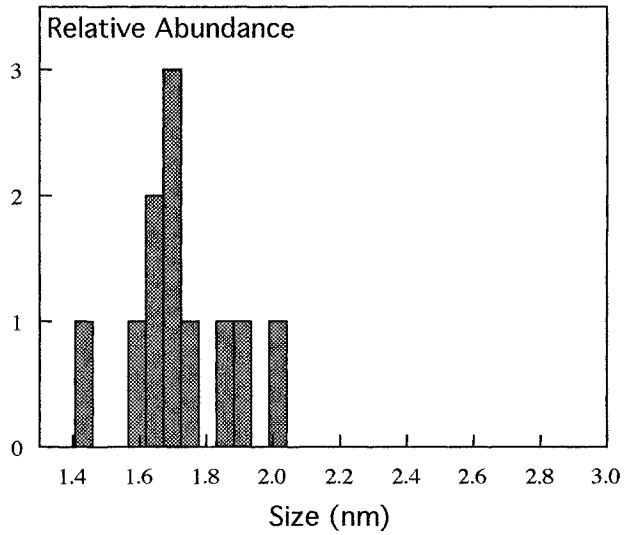

Figure 9. Histogram of the particle-size distribution from figure 6.

Acknowledgement

We are grateful to Professor D.B. Williams, Lehigh University, for granting permission to one of us (VJK) to have access to the VG HB 603 STEM instrument. We are also grateful to Professors C.J. Humphreys and B.F.G. Johnson, and Dr. D.S. Shephard for their interest and help. Parts of this work were supported by grants from Unilever Plc (to JMT and CJH), EPSRC (to VJK) and an EPSRC rolling grant (to JMT).

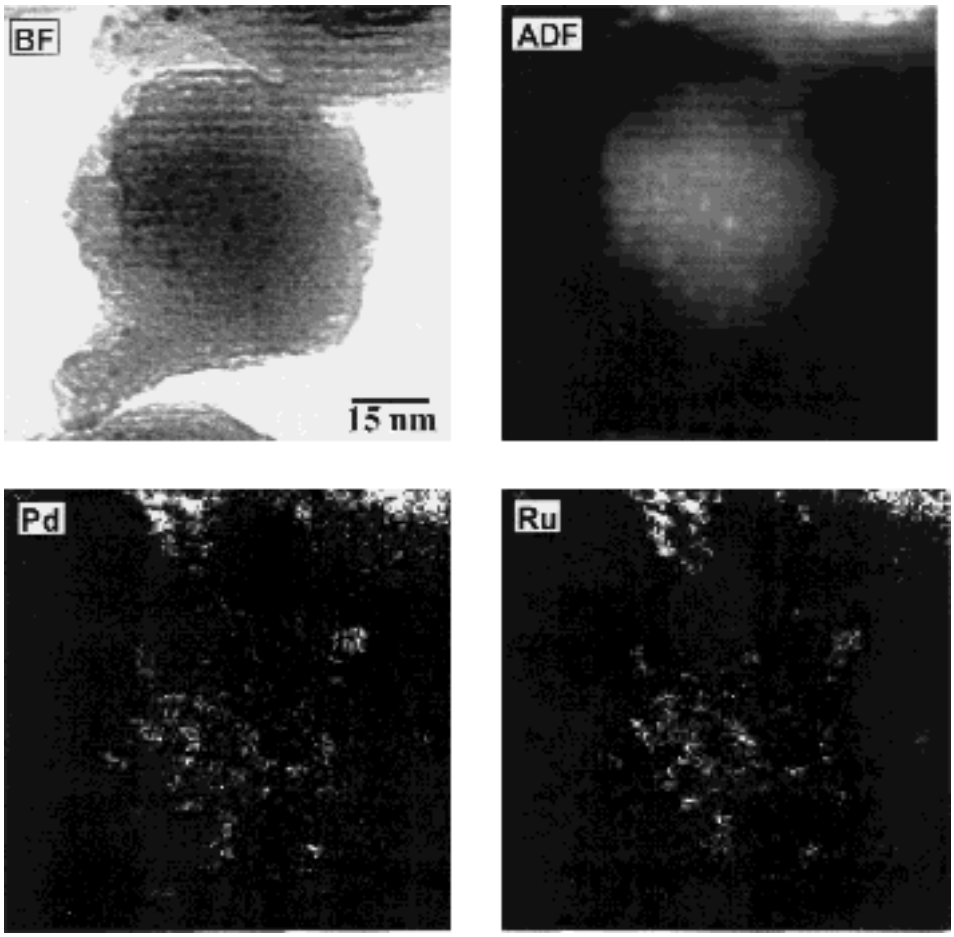

Figure 10. BF and ADF images of MCM-41 with Pd_6Ru_6 particles from VG HB501 STEM (top). Corresponding electron-stimulated X-ray emission images showing Pd and Ru distributions.

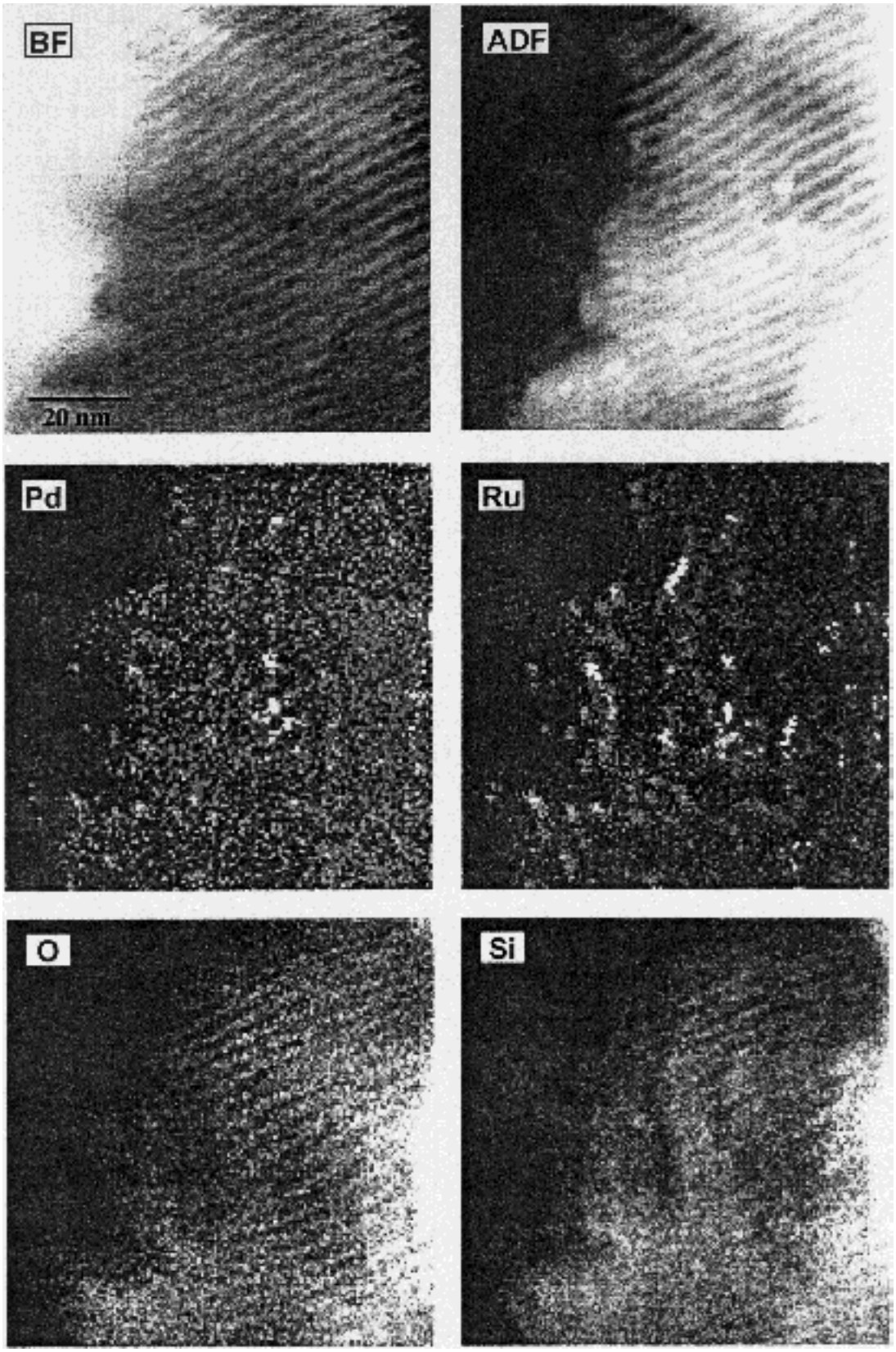

Figure 11. BF and ADF images of MCM-41 with Pd_6Ru_6 clusters, acquired on the VG HB 603 STEM with X-ray emission images from the Pd L_α line, the Ru L_α line, the O K line and the Si K line.

References

[1] C.T. Kresge, M.E. Leonowicz, W.J. Roth, J.C. Vartuli and J.S. Beck, Nature 359 (1992) 710.

[2] J.S. Beck and J.C. Vartuli, Curr. Opin. Solid State Mater. Sci. 1 (1996) 76.

[3] P.D. Yang, T. Deng, D.Y. Zhao, P.Y. Feng, D. Pine, B.F. Chmelka, G.M. Whitesides and G.D. Stucky, Science 282 (1998) 2244.

[4] W. Zhou, H.M.A. Hunter, P.A. Wright, Q. Ge and J.M. Thomas, J. Phys. Chem. 102 (1998) 6933.

[5] T. Maschmeyer, F. Rey, G. Sankar and J.M. Thomas, Nature 378 (1995) 159.

[6] I.J. Shannon, T. Maschmeyer, R.D. Oldroyd, G. Sankar, J.M. Thomas, H. Pernot, J.P. Balikdjian and M. Che, J. Chem. Soc. Faraday Trans. 94 (1998) 1495.

[7] D.S. Shephard, T. Maschmeyer, B.F.G. Johnson, J.M. Thomas, G. Sankar, D. Ozkaya, W. Zhou, R.D. Oldroyd and R.G. Bell, Angew. Chem. Int. Ed. Engl. 36 (1997) 2242.

[8] D.S. Shephard, T. Maschmeyer, G. Sankar, J.M. Thomas, D. Ozkaya, B.F.G. Johnson, R. Raja, R.D. Oldroyd and R.G. Bell, Chem. Eur. J. 4 (1998) 1214.

[9] J.M. Thomas and W.J. Thomas, *Heterogeneous Catalysis: Principles and Practice* (Wiley–VCH, Weinheim, 1997).

[10] J.M. Thomas, Faraday Discuss. 105 (1996) 1.

[11] W. Zhou, J.M. Thomas, D.S. Shephard, B.F.G. Johnson, D. Ozkaya, T. Maschmeyer, R.G. Bell and Q. Ge, Science 280 (1998) 705.

[12] V. Alfredsson and M.W. Anderson, Chem. Mater. 8 (1996) 1141.

[13] D.S. Shephard, R. Raja, S. Hermans, G. Sankar, J.M. Thomas, B.F.G. Johnson and T. Maschmeyer (1999), submitted.

[14] D. Ozkaya, J.M. Thomas, D.S. Shephard, T. Maschmeyer, B.F.G. Johnson, G. Sankar and R. Oldroyd, Elec. Micros. Anal. (1997) 403.

[15] A. Howie, J. Microscopy 177 (1979) 11.

[16] M.M.J. Treacy and A. Howie, J. Catal. 63 (1980) 265.

[17] S.J. Pennycook, Ultramicroscopy 30 (1989) 58.

[18] M.M.J. Treacy and S.B. Rice, J. Microscopy 156 (1989) 211.